Journal of Materials Science & Technology 133 (2023) 12–22

Contents lists available at ScienceDirect

Journal of Materials Science & Technology

journal homepage: www.elsevier.com/locate/jmst

Research Article

Formation process and mechanical properties in selective laser melted multi-principal-element alloys

Jing Peng[a], Jia Li[a,*], Bin Liu[b,*], Jian Wang[c], Haotian Chen[a], Hui Feng[a], Xin Zeng[a], Heng Duan[b], Yuankui Cao[b], Junyang He[b], Peter K. Liaw[d], Qihong Fang[a]

[a] State Key Laboratory of Advanced Design and Manufacturing for Vehicle Body, College of Mechanical and Vehicle Engineering, Hunan University, Changsha 410082, China
[b] State Key Laboratory of Powder Metallurgy, Central South University, Changsha 410083, China
[c] State Key Laboratory of Porous Metal Materials, Northwest Institute for Nonferrous Metal Research, Xi'an 710016, China
[d] Department of Materials Science and Engineering, The University of Tennessee, Knoxville, TN 37996, USA

ARTICLE INFO

Article history:
Received 2 April 2022
Revised 10 June 2022
Accepted 10 June 2022
Available online 9 July 2022

Keywords:
Selective laser melting
Multi-principal-element alloys
Cellular structure
Microsegregation
Grain growth
Mechanical properties

ABSTRACT

Additive manufacturing is believed to open up a new era in precise microfabrication, and the dynamic microstructure evolution during the process as well as the experiment-simulation correlated study is conducted on a prototype multi-principal-element alloys FeCrNi fabricated using selective laser melting (SLM). Experimental results reveal that columnar crystals grow across the cladding layers and the dense cellular structures develop in the filled crystal. At the micron scale, all constituent elements are evenly distributed, while at the near-atomic scale, Cr element is obviously segregated. Simulation results at the atomic scale illustrate that i) the solid-liquid interface during the grain growth changes from horizontal to arc due to the radial temperature gradient; ii) the precipitates, microscale voids, and stacking faults also form dynamically as a result of the thermal gradient, leading to the residual stress in the SLMed structure. In addition, we established a microstructure-based physical model based on atomic simulation, which indicates that strong interface strengthening exists in the tensile deformation. The present work provides an atomic-scale understanding of the microstructural evolution in the SLM process through the combination of experiment and simulation.

© 2022 Published by Elsevier Ltd on behalf of The editorial office of Journal of Materials Science & Technology.

1. Introduction

Selective laser melting (SLM) is a new additive manufacturing (AM) technology, which manufactures materials by tracing the two-dimensional (2D) cross sections of a three-dimension (3D) model layer by layer. Using the high-power laser beam as the energy source, many alloys, such as stainless steels, titanium alloys, and refractory alloys, can be manufactured using SLM [1–3]. Now, SLM has a broad use in the aerospace, biology, and deep sea. SLM is developed from selective laser sintering (SLS) with a much better layer-layer adhesion by remelting the alloy powders [4,5]. The SLM processing parameters, such as the laser power, laser-spot size, scan speed, hatch spacing, hatch style, and layer thickness, have adjustability in a wide range, which has a significant impact on the quality and microstructure of parts [6,7]. Thus, SLM is regarded as an effective means to achieve the target properties of materials. For example, the high laser power and low scanning speed produce high hardness due to the good melting pool quality [5]. The improved surface accuracy and the reduced porosity boost the fatigue performance of the material by adjusting the SLM parameters [6]. By controlling the SLM parameters, 316L SS with a 99% density can be manufactured [8].

Recently, the SLMed multi-principal-element alloys (MPEAs) show high strength, good ductility, and great hardness mechanical properties [9–13]. For instance, the SLMed CoCrFeNiMn MPEA with an almost fully dense structure endows an excellent combination of strength and ductility due to the hierarchical microstructures, such as dislocations, cellular structures, and columnar grains [9–11]. In addition, the synergistic effects of σ phase and nanotwin significantly improve the mechanical properties of the SLMed CoCrFeNiMn [14]. The SLMed FeCoCrNiC MPEAs with fine microstructures and full density have a high yield stress of 656 MPa and a splendid tensile strength of 797 MPa [15]. Meanwhile, the SLM technology combined with the well-controlled annealing effectively reduces the dislocation density and adjusts the cellular structure of MPEA, which is conducive to improving the hydro-

* Corresponding authors.
E-mail addresses: lijia123@hnu.edu.cn (J. Li), binliu@csu.edu.cn (B. Liu).

https://doi.org/10.1016/j.jmst.2022.06.017
1005-0302/© 2022 Published by Elsevier Ltd on behalf of The editorial office of Journal of Materials Science & Technology.

gen embrittlement resistance [16]. In addition, the SLMed FeCrNi MPEA shows the effective combination of the corrosion and mechanical properties due to the Cr segregation along the dislocation cell boundary [17].

In order to explore the dynamic microstructure evolution during the SLM process, the molecular dynamics (MD) simulation can be used as a powerful auxiliary tool to reveal the underlying mechanisms on the nanoscale. The MD simualtion provides the nanoscale microstructure evolution with a sharp temperature change at several microseconds, but this result can hardly be measured by the traditional experiment [18]. For example, the MD simulation shows the dynamic nucleation and the grain growth at the molten pool boundary [19]. The cooling rate effect on the mechanical behavior of the AlCoCrCuFeNi MPEA is investigated by MD simulation [20].

Although the mechanical properties of the SLMed MPEAs have been investigated [21–23], their real-time microstructure evolution and influence mechanisms during SLM progress are rarely revealed at the nanoscale. To solve this issue, we fabricated the sheet sample of SLMed FeCrNi MPEA, and systematically analyzed the microstructures. Meanwhile, based on the results of experimental characterization, the evolution of dynamic microstructure during SLM process was investigated at the nanoscale using an atomic simulation, and then the relationship between the microstructure and mechanical properties was further studied. In the present work, the experiment combined with MD simulation offers an intuitive perspective for studying the local forming process of the SLMed FeCrNi.

2. Methods

2.1. Experimental methods

The near-spherical FeCrNi MPEA powders with an average diameter of 17.9 μm were prepared by the high purity Ar gas atomization. By using the inductively coupled plasma mass spectroscopy (ICP-MS) and instrumental gas analysis (IGA), the element composition of the powder was measured, which contains $Fe_{32.39}Cr_{35.12}Ni_{31.58}$ (at.%), and less than 0.1% C and O. The FS271M machine (Farsoon, Inc, China) was used to execute the SLM process under Ar gas atomization, and the sheet samples with dimensions of 60 nm × 8 nm × 2 mm were built to study the microstructure. The parameters of SLM were listed in Table 1. Meanwhile, in order to eliminate the residual stress, the SLMed samples were further annealed at 400 °C for about 3 h.

The scanning electron microscopy (SEM) equipped with an electron backscatter diffraction (EBSD) analyzer and transmission electron microscopy (TEM, Talos F200X) were used to characterize the microstructure. The distribution of the chemical elements was analyzed by an electron probe micro-analyzer (EPMA, JXA-8530F) on the macro scale, and then was further obtained by using atom probe tomography (APT, LEAP 3000X-HR) on the microscale. The samples used in APT were prepared in a dual-beam focused-ion-beam (FIB)/SEM instrument.

2.2. Computational methods

The MD method is used to investigate the formation process and mechanical properties of SLMed FeCrNi on the atomic scale. Fig. 2 shows the MD model for the SLM process, which comprises an FCC spherical powder and substrate. The substrate contains three grains with the randomly distributed Cr, Fe, and Ni atoms, which is set as the boundary layer, thermostat layer, and Newton layer. The boundary layer at the bottom of the substrate is set to fix the substrate and eliminate motion; the thermostat layer is sandwiched between the boundary layer and the Newton layer. The initial temperature of the system is 293 K, considering that the energy is added to the simulation system during the SLM process. The thermostat layer is kept at a constant temperature of 293 K using the velocity rescaling method, which adjusts the system temperature by rescaling the particle velocity at each time step [24]. The motion of the thermostat layer and Newton layer follows the classical Newton's second law, and their motion can be numerically integrated by the well-established velocity-Verlet algorithm with a time step of 1 fs [25]. In addition, a quarter sphere with a radius of 11.5 nm is selected as the powder in the current work for reducing the amount of calculation under the premise of meeting the accuracy, in which the Fe, Cr, and Ni atoms are randomly distributed with the equal concentrations. Compared with the SLS technology, SLM has the ability to completely melt the powder and produce components with higher density, which can eliminate the effect of the initial crystal structure for the powders [4]. Thus, for the simulation of the complete melting process, the orientations of powder are set to x – [1 0 0], y – [0 1 0], and z – [0 0 1], respectively. For the whole model, the shrink-wrapped boundary conditions are applied in the z-direction. The periodic boundary conditions are set along the x-direction and y-direction to reduce the influence of the length scale.

The embedded atom method (EAM) potential [26–28] has been employed to characterize the FeCrNi MPEA, which has been used to describe the phase transformation, melting process and the deformation behaviour of MPEA [18]. The basic physical properties of the MPEA obey the rule of mixture [29]. Hence, the melting point can be calculated as: $T = \sum_{i=1}^{n} c_i T_i$, where c_i is the atomic percentage, and T_i is the melting point of each element. Therefore, the melting point of the equal atomic FeCrNi MPEA is about 1,850 K. The system is equilibrated under the microcanonical ensemble (NVE) during the whole simulation process [19]. The whole simulation process consists of three parts: the relaxation process, laser heating process, and cooling/solidification process. Firstly, the system is placed at 293 K for the natural relaxation for 400 ps and relaxed to equilibrium configurations. Then, by simulating the effect of the laser energy, the powder is heated to 2,500 K in 200 ps with a constant heat rate to ensure that the powder melts sufficiently. Due to the solidification structures depending on the cooling rates, according to the previous work [20], in order to ensure the formation of complete crystal structure in SLM, the temperature of the molten pool is decreased from 2500 K to 300 K in 350 ps with uneven cooling rate. Considering the influence of the light spot tail on the molten pool with the laser moving, the initial cooling rate is set to be small. After all the simulation process, a SLMed FeCrNi MPEA with a size of 23.857 nm × 23.857 nm × 12 nm is obtained. Although the current SLM simulation only considers the simple thermal-mechanical conditions, the dynamic process of melting and solidification could be revealed at the nanoscale. Similar measure has been taken in previous studies [18,19,30]. For example, the change of atomic-scale structure during the SLM process is investigated by the MD method [18,30]. The local melting, solidification and grain growth process are simulated by the direct control of the temperature at the atomic scale [19].

Table 1
Processing parameters of SLM.

Scanning speed (mm s^{-1})	Laser power (W)	Laser spot diameter (μm)	Hatching space (μm)	Layer thickness (μm)	Scanning rotation angle (°)
700	350	90	110	50	67

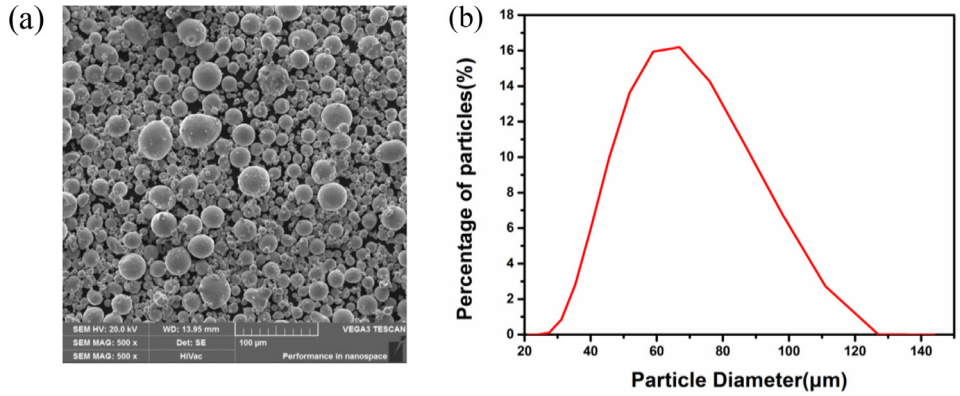

Fig. 1. (a) General morphology of the pre-alloyed FeCrNi MEA powders. (b) Size distribution of the powder particles.

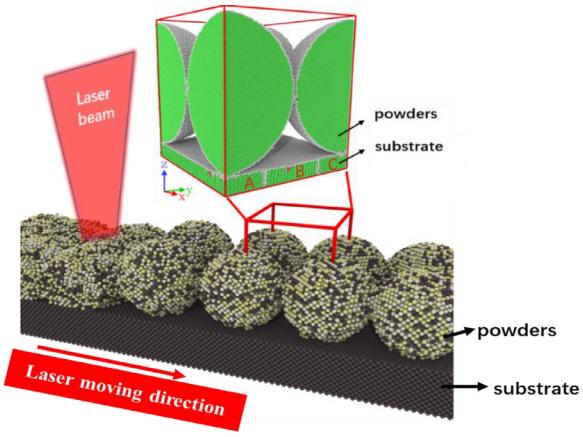

Fig. 2. Atomic model of the SLMed FeCrNi MPEA. The local region of atomic model is highlighted in the red box based on the crystal structure.

In order to investigate the mechanical properties of the SLMed FeCrNi, the cuboid structure is obtained from the whole solidification model by removing the uneven surface and substrate. The structure has a size of 8.03 nm × 23.857 nm × 10.121 nm. Considering that the temperature gradient during solidification produces strong residual stress, the model is annealed [19,31]. The temperature rises to 500 K, keeps for 50 ps, and then slowly decreases to 300 K for eliminating the residual stress and obtaining the initial tensile model. Subsequently, the tensile simulation is applied with the constant strain rate of 1×10^8 s^{-1} along the x and y direction under the Nose'-Hoover isobaric-isothermal (NPT) ensemble with a zero-pressure condition [32]. Periodic boundary conditions are maintained along all directions.

The entire simulation process is based on a large-scale atomic/molecular massively parallel simulator (LAMMPS), and then processed using open visualization tool (OVITO) [33]. To distinguish the microstructures of the SLMed alloys, a common neighbor analysis (CNA) method is used. Here, the green atoms mean face-centered-cubic (FCC) structure, red atoms indicate a hexagonal-close-packed structure (HCP) structure, blue atoms represent a body-centered-cubic (BCC) structure, and gray atoms denote other structures, like liquid and amorphous structures. The dislocation extraction algorithm (DXA) method is used to distinguish the dislocation.

3. Results and discussion

3.1. Experimental characterization and analysis

Fig. 3 shows the microstructures of SLMed FeCrNi in detail. The SEM micrograph of FeCrNi MPEA exhibits the melt pool morphology and characteristics of grain nucleation (Fig. 3(a)). The obvious columnar grain is observed at the boundary of melt pool. This reflects the inheritance of crystal orientation across the cladding layer, which is consistent with the previous studies [17,34]. Fig. 3(b, c) shows the grain filled by a large number of the cellular structures. The solidification condition controls the crystal morphology, in which the temperature gradient (G_T) and the rates of grain growth (R) are two key factors. The equiaxed crystals, columnar crystals, and cellular crystals are formed successively with the increase of G_T/R at a fixed solute concentration [17]. Based on the previous studies [35], the cellular boundary is a dislocation wall composed of the piled and tangled dislocation, which results in a misorientation angle of 1°-2° between the cellulars. The EBSD inverse-pole figure (IPF) map indicates the grain orientation marked by different colors, as shown in Fig. 3(d). There is a slight and continuous transition of grain orientation inside the single grain due to the existence of cellular structure [8,36]. A large proportion of the low-angle grain boundaries (LAGBs) are recognized from the EBSD IQ map in Fig. 3(e). Meanwhile, according to the statistical results of grain boundaries (GBs) line length in Fig. 3(f), the fraction of low-angle GBs exceeds 50% of total GBs. The TEM bright images in Fig. 3(g, h) show the dislocation wall and residual dislocations as well as stacking faults (SFs) in the SLMed FeCrNi MPEA. It is noted that the stacking fault energy (SFE) would affect the deformation mechanisms of MPEA [32]. Here, SFE obtained from our MD simulation is 27 mJ/m^2 for the FeCrNi MPEA, as shown in Fig. 3(i). Thus, partial dislocations are more likely to occur compared to full dislocations [32,37]. In other words, SFs can easily take place in the SLMed FeCrNi MPEA.

To investigate the chemical composition distribution, the EPMA results indicate that the elements are evenly distributed on the micron scale without obvious segregation (Fig. 4(a)). Further analysis of the element distribution is performed by APT at near-atomic scale (Fig. 4(b)). The element composition along the black dotted line is shown in Fig. 4(c). The characterization and measurement results show the significant Cr and C element enrichment area in the red box. According to the previous study [38], the interstitial atoms diffuse faster than principal elements, so the interstitial atom C is the first to modify the boundary according to the fast diffusion kinetics. According to the mechanisms of Bernard Marangoni driven instability and the particle accumulated structure formation [39], the solubility of Cr atoms with high melting point decreases in a solvent at a high cooling rate, which is ejected and aggregated along the interface driven by surface tension. Combined with the thermodynamic mechanism of cellular structure formation [17,35], the interfaces of the element aggregation are cellular boundaries. Meanwhile, the content of the C element in the SLMed FeCrNi accounts for a small proportion, and thus the main element is Cr in the segregation area. This phenomenon is

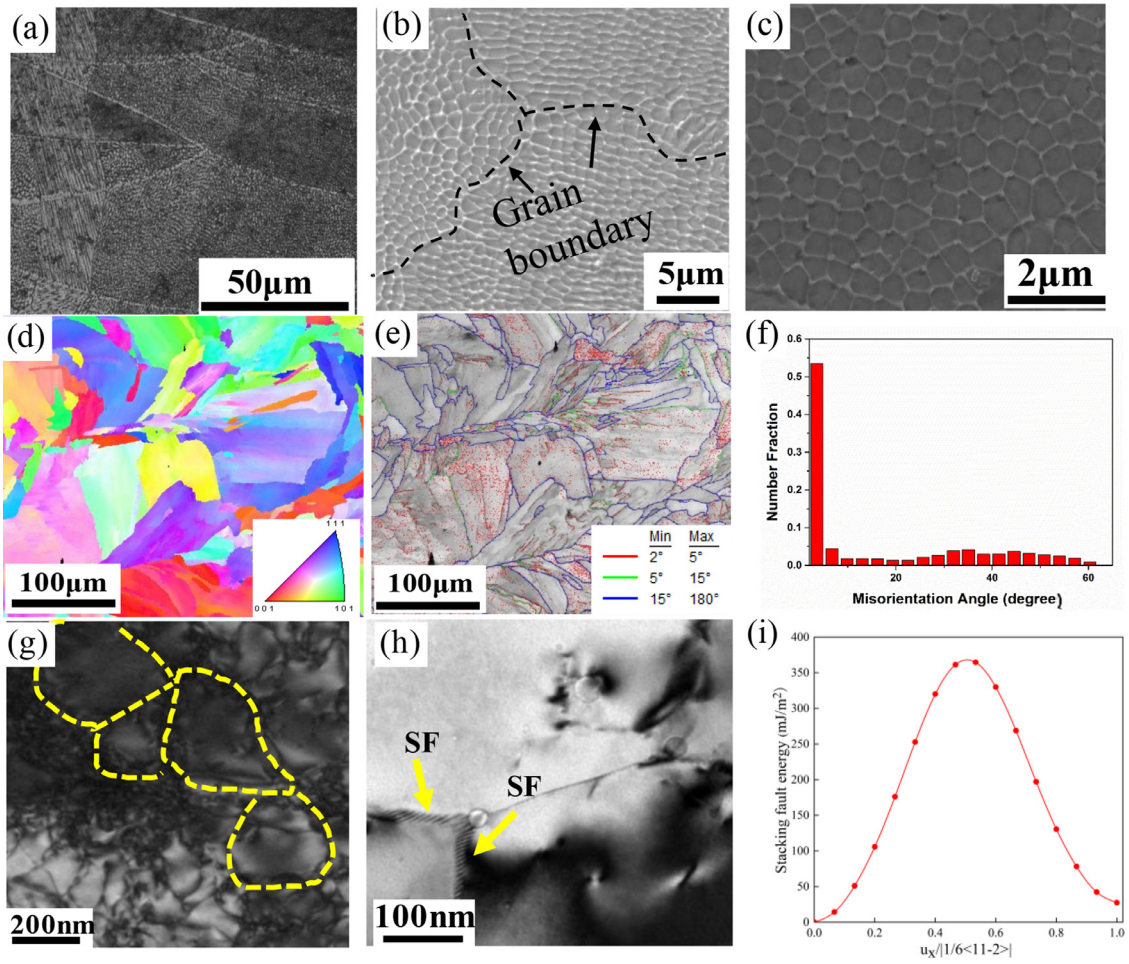

Fig. 3. (a) SEM micrograph of SLMed FeCrNi MPEA. (b, c) SEM micrographs of showing the cellular structure inside the grain. (d) EBSD IPF map, and (e) EBSD image quality (IQ) map superimposed with HAGBs and LAGBs. (f) Numerical statistics of the misorientation angle. For the SLMed FeCrNi, TEM images of (g) residual dislocations and (h) SFs. The yellow dashed lines represent the dislocation walls. (i) SFE as a function of the normalized Burgers vector in FeCrNi MPEA.

related to different melting temperatures between the constituent elements [8,40].

Fig. 5(a) shows the tensile engineering stress-strain curves of the SLMed FeCrNi at room temperature, where the results of SLMed 316L and as-cast FeCrNi are added for the comparative analysis [17,41]. The yield stress of the SLMed FeCrNi is 750 MPa, which is five times that of the as-cast FeCrNi, and 1.5 times that of the SLMed 316L. Meanwhile, the excellent ultimate strength and elongation of the SLMed FeCrNi are reflected. The TEM bright-field images in Fig. 5(b) show the piled-up dislocations at the cellular boundary and the SFs after the plastic deformation. The pinning effects of dislocation wall and element segregation on the dislocation slip would enhance the strength of SLMed FeCrNi.

3.2. Atomic simulation

On the basis of the difference in element distribution between the micron scale and the near-atomic scale, the melting and solidification processes during SLM at the atomic scale are carried out by the MD method, in order to further explore the influence of microstructure. The dynamic columnar crystal growing process is observed, and the microstructure characteristic of SLMed MPEA is revealed by analyzing the element distribution and defect evolution in the SLM process. To further analyze the mechanical properties of SLMed MPEA, the tensile simulation is implemented. The results are compared with the calculation results of the physical model based on the microstructure characteristics.

3.2.1. Columnar crystal growth mechanism

The melt pool morphology and the columnar crystal growing process are exhibited in this section. Fig. 6 shows the cooling temperature and the microstructure during the melting and solidification. The average value of the heating rate and cooling rate is 11 K/ps and 6.3 K/ps, respectively (Fig. 6(a)). The energy of the laser beam heats the solid alloy into a liquid state, and the initial microstructure and the element distribution of the powder are destroyed. Fig. 6(b-e) reveals the microstructure evolution and temperature distribution during the melting process with a duration of 200 ps. At the beginning, the energy from the laser beam heats the surface of powders into a liquid state while the central region remains a solid state. In Fig. 6(c), the surface of the powder in a cross-sectional view is transformed into gray, and the temperature of the powders increases significantly. Then, the average height of the model decreases due to that all powders are melted and fill the gap between powders under the action of gravity. At t = 200 ps, the melting process is completed, and a melted pool over 17 nm is formed. The highest temperature is over 2,500 K at the surface of the melted pool, which has a near-linear temperature variation along the z-direction from Fig. 6(e).

Fig. 6(f-j) shows the surface morphology evolution and grain-growth process of the molten pool during solidification. The temperature-time relationship for the whole cooling process from 200 to 550 ps is shown in Fig. 6(a), where the maximum cooling rate is 7.5 K/ps at 350 ps. In order to quantitatively compare the formation of the solid-liquid interface of the molten pool in

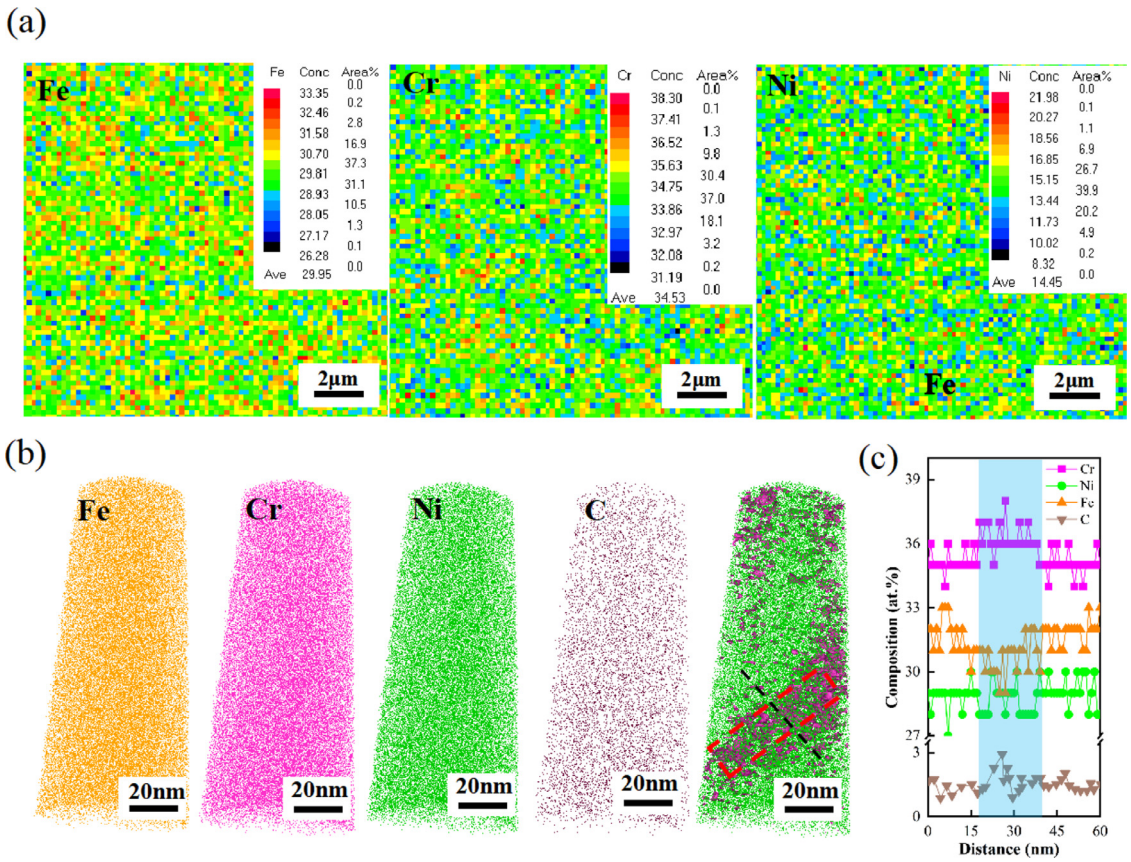

Fig. 4. (a) EPMA results of element distribution in the macro-scale of SLMed FeCrNi, (b) APT image of local chemical information at near-atomic scale, where the obvious element segregation is shown in the red dashed box. (c) Element composition measured along the black dotted line.

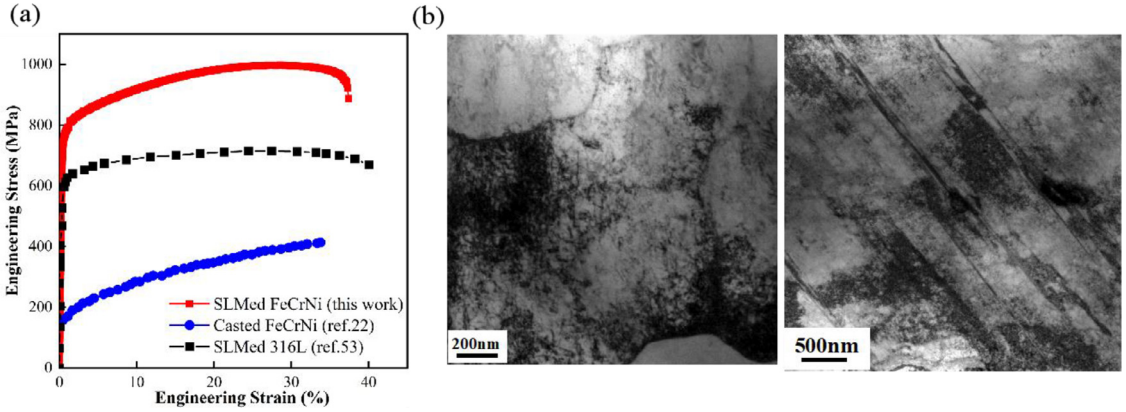

Fig. 5. (a) Stress-strain curves of the SLMed FeCrNi, the casted FeCrNi [17] and the SLMed 316L [40]. (b) TEM bright-field images after deformation.

the solidification process, the cooling rate is set as a relatively-constant value to eliminate the interfering factors. Here, the cooling rate used is based on the previous studies using MD simulation [20]. Based on the SLM technology, it can be known that the solidification process of the molten pool is mainly affected by two key effects: the heat conduction of the solid-liquid interface of the molten pool, and the heat dissipation of the substrate. Compared with Fig. 6(e), the depth of the molten pool is over 15 nm, and then decreases at $t = 250$ ps (Fig. 6(f)). The red arcs describe the location of the solid-liquid interface (Fig. 6(f-i)), and the red arrows indicate the direction of the grain growth and heat flow, which is perpendicular to the solid-liquid interface [42]. The phenomenon shows the transformation from the longitudinal thermal gradient to the radial thermal gradient during the solidification. With the decreased temperature and the columnar grain growth (Fig. 6(g)), the depth of the pool decreases further. The solid-liquid interface gradually changes from the initially-flat straight line to a curved arc (Fig. 6(g)); thus, the solid-liquid interface protrudes upward in the middle of the grain and bends downward near the GB, due to the difference in liquid penetration [43].

By comparing Fig. 6(h) and (i), it can be found that the bending degree of the solid-liquid interface increases due to the high capillary force [44]. The growth rate (solidification rate) of grains at the solid-liquid interface is obviously different, and the growth rate at the center of the grain is significantly higher than that near the GB. At 430 ps, the solidification process has been completed at the center of the grains (Fig. 6(i)), while there is still a molten pool of partially-melted metals near the GB. At the same time, the size of the molten pool is very small, and the viscosity of the fluid increases with the decrease of the temperature. Hence, the solidi-

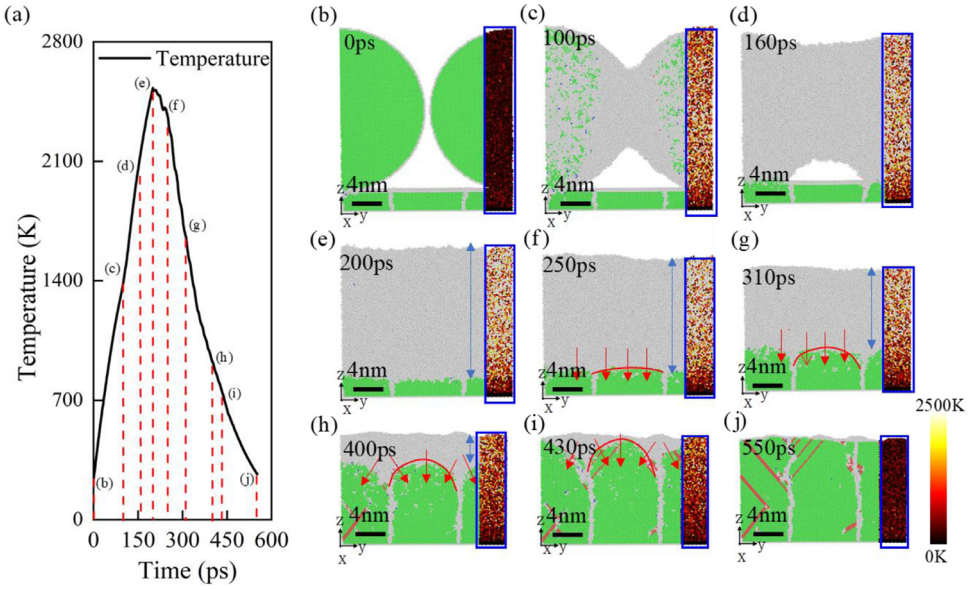

Fig. 6. Melting and solidification process. (a) Cooling temperature of melt pool with the increased time. The cross-section view of the model for the different time: (b) 0, (c) 100, (d) 160, (e) 200, (f) 250, (g) 310, (h) 400, (i) 430, and (j) 550 ps. The atoms in the blue box are colored by the temperature, and the atoms out of the blue box are colored by the atomic structure. The red arrows show the direction of heat conduction, and the red arcs show the boundary of the columnar crystal, and the blue arrows indicate the depth of the molten pool.

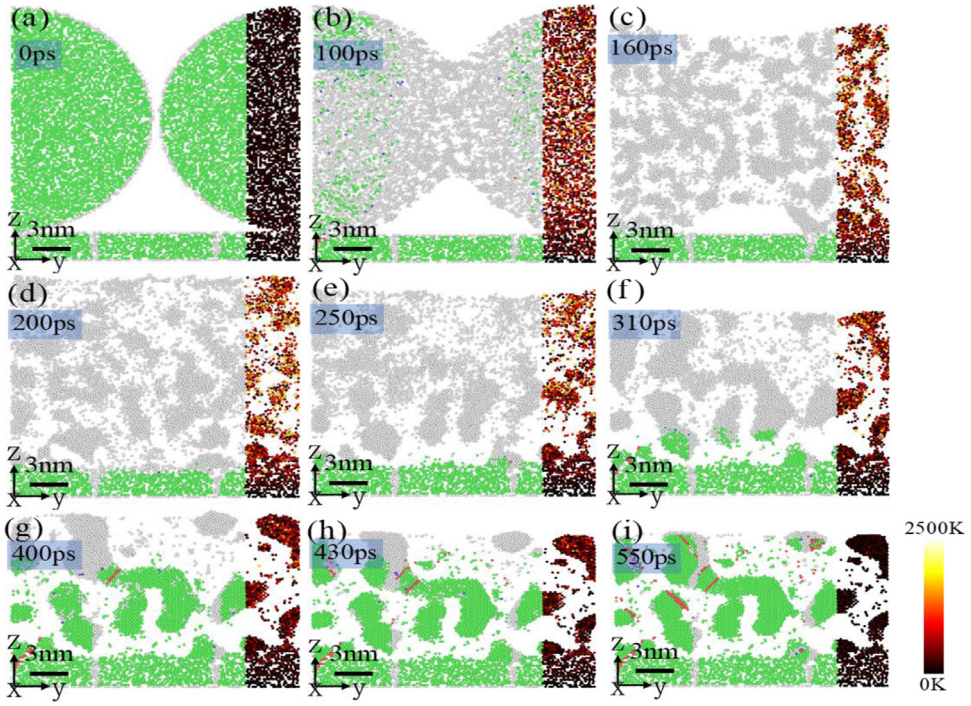

Fig. 7. Cr-elemental distribution during the SLM process. The cross-section views of the model at the different time: (a) 0, (b) 100, (c) 160, (d) 200, (e) 250, (f) 310, (g) 400, (h) 430, and (i) 550 ps. The atoms in the right part are colored by the temperature, and the other regions are colored by the atomic structure.

fication rate decreases significantly, and many defective structures generated after the solidification are located at the GB.

3.2.2. Formation of Cr-rich cluster

In order to investigate the elemental distribution during SLM, the slice in the [100] direction is taken out, and the Cr distribution during the melting and solidification process is displayed in Fig. 7. According to the previous work [8,40], elements with a high melting point are more likely to form the segregation for SLM. Hence, Cr-rich clusters are observed in the MD simulation. The Cr atoms do not fully enter the melting state before 200 ps, so they cannot overcome the motion resistance to form obvious segregation (Fig. 7(a-d)). The Cr elemental distribution in the initial solidification state at 250 ps is exhibited in Fig. 7(e), and the Cr segregation depends upon the temperature sensitivity [17]. At this time, the temperature just exceeds the melting temperature at the boundary of the molten pool near the substrate, due to the farthest distance from the laser and the heat dissipation of the substrate. The Cr-rich cluster has a clear outline and stable structure. However, the surface is greatly affected by the laser energy, and the local temperature is much higher. Thus, the outline of clusters is fuzzy without a clear boundary.

In addition, from Fig. 7(e-i), the obvious longitudinal deposition phenomenon can be found, and the partial polymerization of Cr on

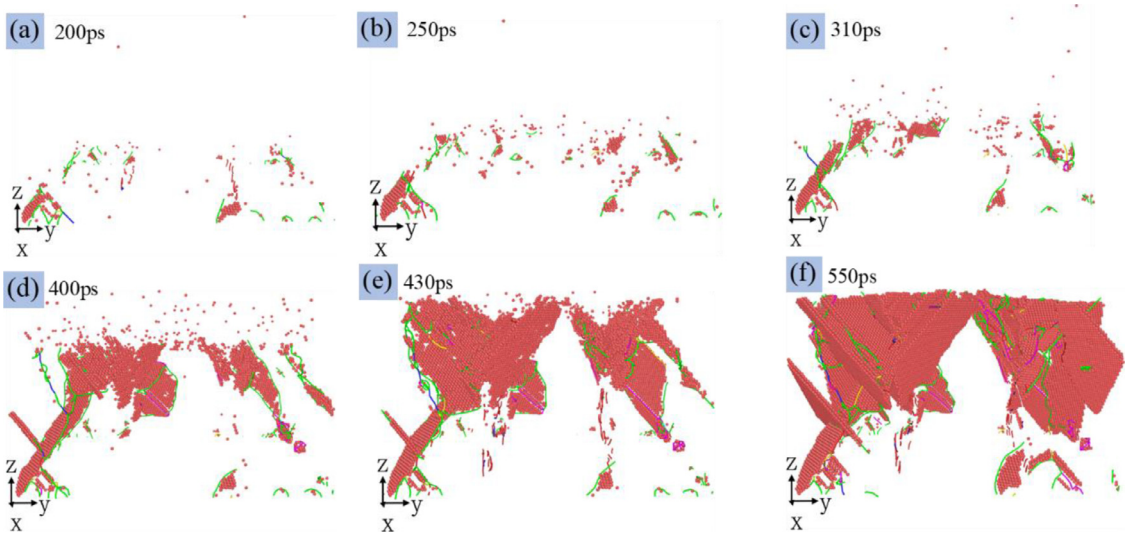

Fig. 8. Distribution of the dislocation and the SFs for the different time: (a) 200, (b) 250, (c) 310, (d) 400, (e) 430, and (f) 550 ps. Here, the red atoms represent HCP structure, the green line represents the 1/6<112> Shockley dislocation, the pink line is the 1/6<110> stair-rod dislocation, the blue line denotes the 1/6<110> perfect dislocation, the sky-blue line is the 1/3<111> frank dislocation, and the red line is other dislocations.

the surface of the pool is obviously weaker than that at the bottom of the pool. Moreover, the surface of the pool is melted first by the laser beam, and its duration is longer than that at the bottom of the pool. Thus, the Cr segregation is not related to the duration of high temperatures. The mutual attraction force between Cr atoms cannot overcome the energy of Brownian motion at high temperatures, leading to the disordered structure [45]. However, after the temperature drops, the driving force of partial polymerization gradually dominates, and the phenomenon of partial polymerization occurs. The temperature and solidification time of the molten pool can be adjusted to control the appearance of partial polymerization. The temperature of traditional manufacturing of a stainless steel is less than 2,000 K. The MD results show that when the temperature is close to 3,000 K, the Cr segregation is inhibited. The characteristics of rapid cooling during SLM can complete the solidification and cooling process in a short time. Thus, the Cr segregation is controlled on picosecond and nanometer scales, which plays an important role in impeding the destruction of high Cr concentrations to the material. On the other hand, there are significant differences between the liquid and solid MPEAs. Meanwhile, the Cr segregation occurs in the phase transition from the liquid state to the solid state, rather than from solid to liquid. The degree of freedom of the atoms is greatly improved in the liquid phase, which enables the Cr atoms to form Cr-rich cluster with significant segregation at the nanometer scale in a very short time (several picoseconds). At the same time, Cr atoms at high temperatures but not in the melting state could not overcome the resistance of motion. Thus, no obvious biased structure appears.

3.2.3. Dynamic evolution of defects

The evolution of the dislocations and SFs for the solidification is exhibited in Fig. 8. The powders are melted completely until the time is 200 ps. The solid-liquid interface above the intermediate grain is not formed before 160 ps, because the cavity between the powders is not filled (Fig. 8(c)). The columnar crystals begin to form after 200 ps. Meanwhile, the dislocation and SFs are gradually generated due to the initial dislocation in the substrate grain as the dislocation sources with the growth of columnar crystals. The GB has to accommodate the misfit through a GB dislocation [46]. The scattered HCP structures are formed and can be used as new dislocation emission sources at the junction of the GB and solid-liquid interface at the initial stage of solidification.

In addition, the dislocation nucleation and propagation related to the solid-liquid interface, the dislocation propagates laterally and the SF plane is expanded under the action of thermomechanical multiaxial stress [47]. Due to the effect of the radial thermal gradient, the dislocations are emitted from the multiple different sources that enter into the grain; and the Shockley partial dislocations slip in the slip planes {111}, resulting in the significant expansion of the SFs plane after 400 ps. The 1/6<110> stair-rod partial dislocation is another major type of dislocations, and contributes higher strength due to its immovable characteristics. As the grain growth proceeds, the dislocation propagates, and the direction is always perpendicular to the normal direction of the solid-liquid interface.

3.2.4. Tensile property

In this section, the mechanical properties of the SLMed MPEA are investigated. The structure contains three grains (Fig. 9). Due to the rapid melting and solidification, a large residual stress is generated [48]. Thus, the annealing treatment is applied for reducing the inevitable residual stress and micro defects before the tensile simulation. For the tensile simulation, the strain rate of 1×10^8 s^{-1} is applied. The distribution of microstructures before and after annealing is shown in Fig. 9. Compared with Fig. 9(a, c) and 9(b, d), the discrete amorphous atom clusters, and the discrete gray patches in grains represent the porosity formed in laser processing, which are partially eliminated by the dislocation emission and atomic diffusion during the process of annealing. The percentage of amorphous atoms decreases by 2.4%. The percentage of HCP atoms is significantly reduced from 3.8% to 0.7% after annealing (Fig. 9(f)), which reflects the annihilation of SFs and dislocations. However, the effect of annealing on atom distributions is very weak. Thus, the morphology of the Cr-rich cluster is basically unchanged (Fig. 9(e, f)).

In Fig. 10(a), the red line shows the stress-strain curves in the *x*-direction, and the black line shows that in the *y*-direction. The yield stresses along the *x* and *y* directions are 5.1 and 4.78 GPa, respectively. Compared with the *y*-direction, the yield stress in the *x*-direction is larger, and there is an obvious hardening phenomenon. The reason is attributed to the microstructure. Fig. 10(b, c) represents the microstructure at the yield point for tension in the *x* and *y* directions. Though the residual stress is eliminated by annealing, some defects, such as the dislocations and small voids, are still retained, as presented in Fig. 9(d, g). The residual dislocation

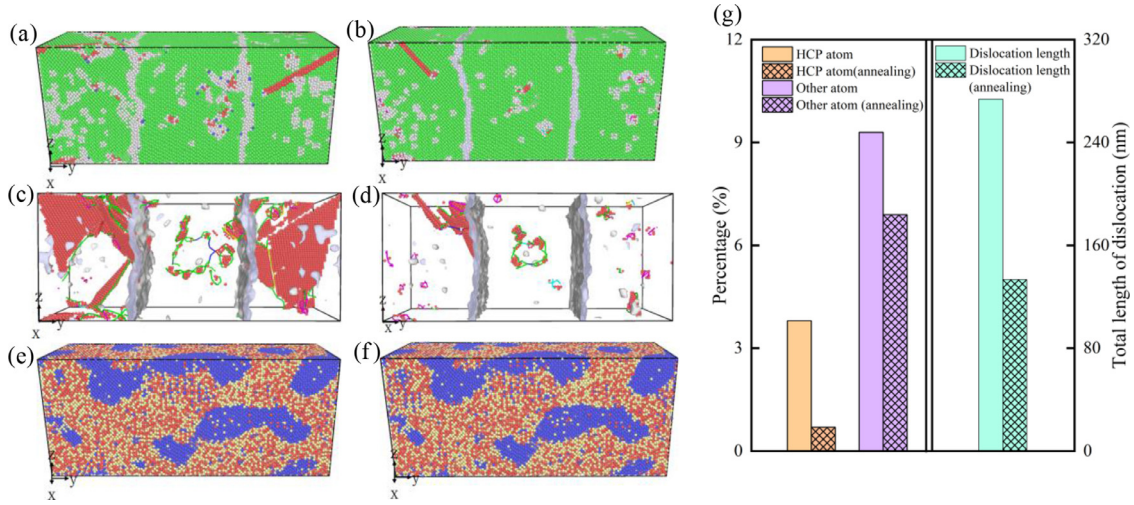

Fig. 9. (a, b) Snapshots of the microstructures before and after annealing. (c, d) Defects before and after annealing. (e, f) Elemental distribution before and after annealing, where Cr, Fe, and Ni. (g) Percentages of HCP and other atoms, and total length of dislocation before and after annealing.

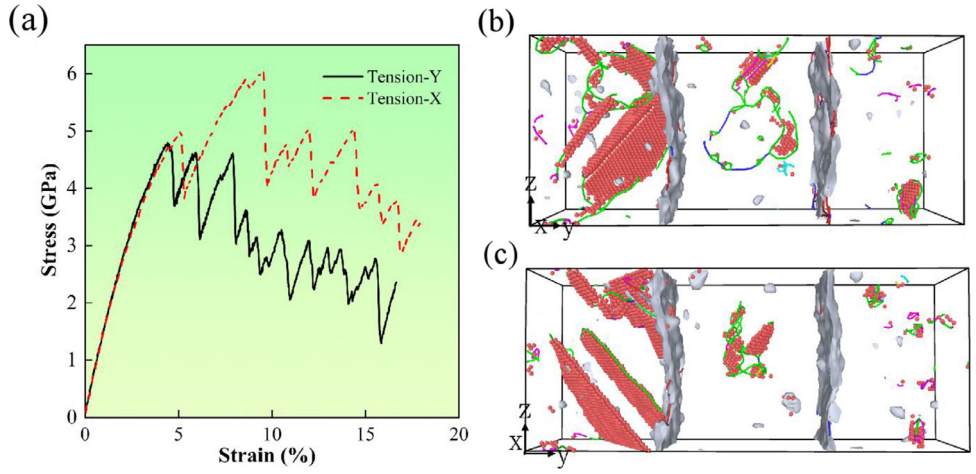

Fig. 10. (a) Stress-strain curves along *x* and *y* loading directions. The microstructures for (b) *x* loading direction and (c) *y* loading direction at the yield point.

proliferation and slip lead to the SLMed FeCrNi to yield. Due to the difference of angle between the direction of the GB and the loading direction, the GB strengthening effect is significantly different. The nucleation of interfacial dislocation plays an important role in plastic deformation and yield strength [46]. According to the statistics of DXA method, in order to adapt to the plastic deformation, many interfacial dislocations are generated in the interface, and the density of interfacial dislocations induced by stretching along the *x*-direction is 3.8 times that along the *y*-direction. Meanwhile, in order to investigate the effect of the sample size, the corresponding stress-strain curves of SLMed FeCrNi MPEAs are computed (Fig. 11), which show that the yield strength from 4.90 GPa to 5.38 GPa with the increase of sample size. The results show the yield strength increases with the decrease of the sample size. This trend is consistent with the previous results for "the smaller is the stronger" [49].

4. Microstructure-based strength model

Based on the MD simulation results and microstructure characteristics, in this section, a microstructure-based physical model is established to calculate the contribution of microstructure to strength. This model can be considered as a nano-layered structure. The thickness of the layer is much less than 50 nm, and the strength caused by the interface cannot be calculated according to the traditional Hall-Petch relationship [50]. Therefore, considering the interface itself and the interaction between dislocation and interface [51], the interface strengthening mechanism can be expressed as:

$$\sigma_b = M\frac{\mu b_p \sin\theta}{8\pi t}\left(\frac{4-\upsilon}{1-\upsilon}\right)\ln\left(\frac{\alpha t}{b_p \sin\theta}\right) - \frac{F}{t} \quad (1)$$

where M is Taylor factor, μ is shear modulus, b_p is the magnitude of Burger vector of partial dislocation, θ is the angle between slip plane and interface, t is thickness, υ is Poisson's ratio, α is the dislocation core cut-off parameter with a range of 0-1, and F is the characteristic interface stress of multilayers [51].

In addition, for MPEAs, lattice distortion is also one of the strengthening mechanisms [52]. According to the Vegard's law [53], lattice distortion strengthening can be written as:

$$\sigma_s = \sum c_i \sigma_s^i \quad (2)$$

where the c_i is the concentration of element *i*, and its contribution to the total elementσ_{ss}^i can be written as:

$$\sigma_s^i = A\mu c_i^{2/3}\delta_i^{4/3} \quad (3)$$

where A is a material constant and its value is 0.04 [54]. The shear modulus μ follows the average rule [29]. The mismatch parameter

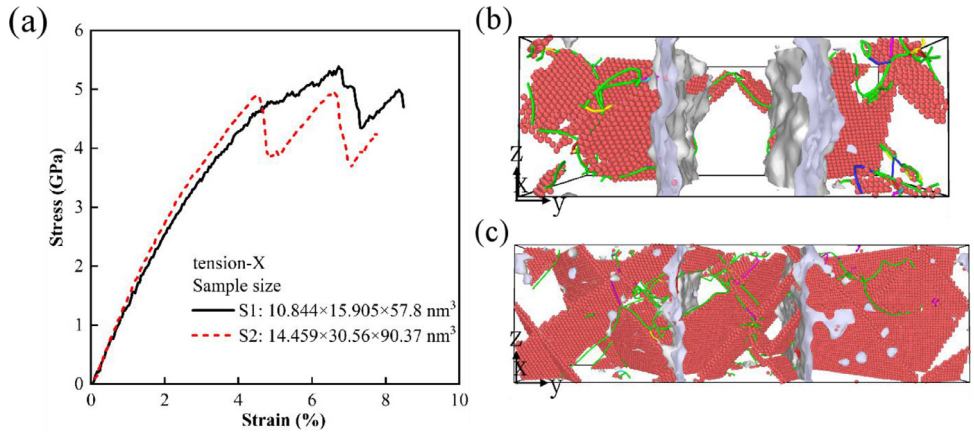

Fig. 11. (a) Stress-strain curves of SLMed FeCrNi MPEAs with different simulation cells. The microstructures for samples (b) S1 and (c) S2 at the yield point.

δ_i consists of the shear modulus mismatch $\delta\mu_i$ and volume mismatch δr_i.

$$\delta_i = \xi\left(\delta\mu_i^2 + \beta^2\delta r_i^2\right)^{1/2} \tag{4}$$

where $\xi = 1$ in FCC metals [54], and the value of β depends on the type of dislocation, which is 16 in the present work [54]. $\delta r_i = \frac{\delta r_{ijk}^{ave} - \delta r_{jk}^{ave}}{c_i}$, $\delta\mu_i = \frac{\delta\mu_{ijk}^{ave} - \delta\mu_{jk}^{ave}}{c_i}$. δr_{ijk}^{ave} and $\delta\mu_{ijk}^{ave}$ Research Article are the average volume mismatch and average modulus mismatch of the *ijk* alloy, respectively. And the average volume mismatch and average modulus mismatch can be written as Eqs. (5) and (6).

$$\begin{aligned}\delta r^{ave} &= \sum_i^n\sum_j^n c_i c_j \delta r_{ij} \\ &= (c_1, c_2, \cdots, c_n)\begin{pmatrix}\delta r_{11} & \delta r_{12} & \cdots & \delta r_{1n}\\ \delta r_{21} & \delta r_{22} & \cdots & \delta r_{2n}\\ \vdots & \cdots & \ddots & \vdots\\ \delta r_{n1} & \delta r_{n2} & \cdots & \delta r_{nn}\end{pmatrix}\begin{pmatrix}c_1\\ c_2\\ \vdots\\ c_n\end{pmatrix}\end{aligned} \tag{5}$$

$$\begin{aligned}\delta\mu^{ave} &= \sum_i^n\sum_j^n c_i c_j \delta\mu_{ij} \\ &= (c_1, c_2, \cdots, c_n)\begin{pmatrix}\delta\mu_{11} & \delta\mu_{12} & \cdots & \delta\mu_{1n}\\ \delta\mu_{21} & \delta\mu_{22} & \cdots & \delta\mu_{2n}\\ \vdots & \cdots & \ddots & \vdots\\ \delta\mu_{n1} & \delta\mu_{n2} & \cdots & \delta\mu_{nn}\end{pmatrix}\begin{pmatrix}c_1\\ c_2\\ \vdots\\ c_n\end{pmatrix}\end{aligned} \tag{6}$$

$\delta r_{ij} = 2(r_i - r_j)/(r_i + r_j)$ and $\delta\mu_{ij} = 2(\mu_i - \mu_j)/(\mu_i + \mu_j)$ are the volume mismatch and shear modulus mismatch between two elements, respectively, where r_i is atomic radii, and the μ_i is shear moduli of element *i*.

The immovable dislocations calculated by DXA method are used as the source of dislocation slip resistance. According to the Taylor relationship [55], the dislocation strengthening can be expressed as:

$$\sigma_d = M\varsigma\mu b\sqrt{\rho} \tag{7}$$

where ς is empirical constant, b is the value of Burgers vector of complete dislocation, ρ is dislocation density. Thus, the total strength can be summarized as:

$$\sigma_{yield} = \sigma_d + \sigma_s + \sigma_b \tag{8}$$

According to the results of MD simulation and previous studies [50,54,56], the parameters of the physical model are listed in Table 2.

Table 2
Parameters of the FeNiCr MPEA [50,54,56].

Parameter	Symbol	Magnitude
Taylor factor	M	3.06
Shear modulus (GPa)	μ	88
Burger vector of partial dislocation (nm)	b_p	0.1476
Burger vector of complete dislocation (nm)	b	0.25
Angle	θ	68.58°
Thickness (nm)	t	8
Characteristic interface stress (J m^{-2})	F	2
Dislocation core cut-off parameter	α	0.1 for *Y*, 0.2 for *X*
Average density of immovable dislocation (m^{-2})	ρ	1.7×10^{16} for *X*, 1.9×10^{16} for *Y*
Empirical constant	ς	0.33
Taylor factor	M	3.06

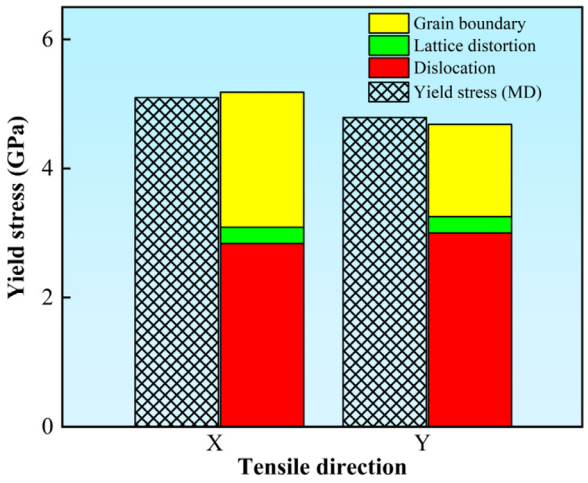

Fig. 12. Comparison of yield stress between MD simulation and physical model in *x* and *y* loading directions. Grid columns represent the yield strength obtained from MD. Color columns represent the contribution of different strengthening mechanisms on yield strength, where the red column is dislocation strengthening, the green column is lattice distortion strengthening, and the yellow column is interface strengthening.

Based on the above derivation, the contribution of every strengthening mechanism to yield stress can be calculated quantitatively and it is exhibited in Fig. 12. The dislocation strengthening and interface strengthening are the main strengthening mecha-

nism. The density of immovable dislocations before the yield point is slightly higher when stretching along the *y*-direction than that in the *x* loading direction. Thus, the dislocation strengthening is slightly higher in the *y*-tension direction. In addition, it can be found that the main reason for the difference of yield strength between the two directions is the interface strengthening mechanism [51,56]. The interfacial dislocation regulates the plastic deformation and enhances the interfacial strengthening effect.

5. Conclusions

In the work, we study the formation process and mechanical properties of the SLMed FeCrNi MPEA using experiment and atomic simulation. The columnar crystal grown across the molten pool and a large number of cellular structures within the grain are observed in the SLMed FeCrNi. By characterizing the distribution of elements at different scales, the elements are evenly distributed on the micron scale, while there is an obvious Cr cluster on the nanoscale. The atomic simulation shows that the nanoscale powder melts completely at a temperature higher than the melting point and fills the gap under the action of gravity to form a homogeneous liquid molten pool. As the molten pool gradually cools, the growth of columnar crystalline is observed at the nanoscale. The shape of solid-liquid interface changes from flat line to arc line, owing to the strong radial temperature gradient and the large viscosity difference. The solidification process is accompanied by the element redistribution, and the Cr segregation is closely related to the temperature gradient. The SFs and small voids are gradually generated with the growth of columnar crystals, which reflects the limitation that the actual SLM technology can not achieve complete densification.

In addition, the proliferation and slip of residual dislocations in grains are dominant plastic deformation in SLMed FeCrNi. The dislocation produced by GB deformation plays a great influence on interface strengthening. Thus, based on the results of simulations, a microstructure-based physical model is established for analyzing the contribution of microstructure to strength. The theoretical calculation results further prove that in addition to the dislocation strengthening, the interface strengthening mechanism is a significant determinant of strength. Through the combination of experiment and simulation, the current research provides insight into the formation mechanism and mechanical properties of SLMed microstructure to develop advanced alloys.

Data availability

The data that support the findings of this study are available from the corresponding author upon reasonable request.

Declaration of Competing Interest

The authors declare that they have no known competing financial interests or personal relationships that could have appeared to influence the work reported in this paper.

Acknowledgments

This work was financially supported by the National Natural Science Foundation of China (Nos. 52020105013, 51871092, and 11902113), the Natural Science Foundation of Hunan Province (Nos. 2019JJ50068 and 2021JJ40032), and the Changsha Municipal Natural Science Foundation (No. kq2014126). **Peter K. Liaw** very much appreciates the support from the National Science Foundation (Nos. DMR-1611180 and 1809640).

Appendix

Fig. A1.

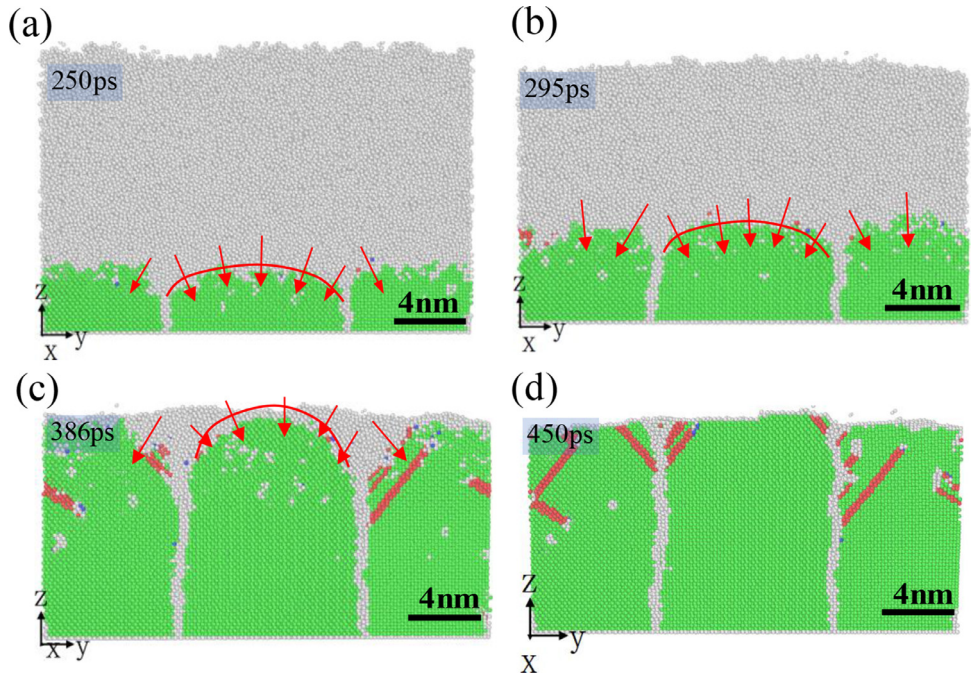

Fig. A1. Grain morphology evolution of a model with random orientation of powder. The cross-section view for different time: (a) 250, (b) 295, (c) 386, and (d) 450 ps.

References

[1] Q. Jia, P. Rometsch, P. Kürnsteiner, Q. Chao, A. Huang, M. Weyland, L. Bourgeois, X. Wu, Acta Mater. 171 (2019) 108–118.
[2] T. DebRoy, H.L. Wei, J.S. Zuback, T. Mukherjee, J.W. Elmer, J.O. Milewski, W. Zhang, Prog. Mater. Sci. 92 (2018) 112–224.
[3] N.J. Harrison, I. Todd, K. Mumtaz, Acta. Mater. 94 (2015) 59–68.
[4] H. Jia, H. Sun, H. Wang, Y. Wu, H. Wang, Int. J. Adv. Manuf. Tech. 113 (2021) 2413–2435.
[5] X. Zhang, Y. Liao, Powder Technol. 339 (2018) 677–685.
[6] B. Nagarajan, Z. Hu, X. Song, W. Zhai, J. Wei, Engineering 5 (2019) 702–720.
[7] I. Koutiri, E. Pessard, P. Peyre, O. Amlou, T. De Terris, J. Mater. Process. Technol. 255 (2018) 536–546.
[8] Y.M. Wang, T. Voisin, J.T. McKeown, J. Ye, N.P. Calta, Z. Li, Z. Zeng, Y. Zhang, W. Chen, T. Roehling, R.T. Ott, M.K. Santala, P.J. Depond, M.J. Matthews, A.V. Hamza, T. Zhu, Nat. Mater. 17 (2018) 63–71.
[9] B. Li, L. Zhang, Y. Xu, Z. Liu, B. Qian, F. Xuan, Powder Technol. 360 (2020) 509–521.
[10] J.M. Park, J. Choe, J.G. Kim, J.W. Bae, J. Moon, S. Yang, K.T. Kim, J.H. Yu, H.S. Kim, Mater. Res. Lett. 8 (2020) 1–7.
[11] Z.G. Zhu, Q.B. Nguyen, F.L. Ng, X.H. An, X.Z. Liao, P.K. Liaw, S.M.L. Nai, J. Wei, Scr. Mater. 154 (2018) 20–24.
[12] Y. Wang, R. Li, P. Niu, Z. Zhang, T. Yuan, J. Yuan, K. Li, Intermetallics 120 (2020) 106746.
[13] J. Li, B. Xie, L. Li, B. Liu, Y. Liu, D. Shaysultanov, Q.H. Fang, N. Stepanov, P.K. Liaw, Mater. Horiz. 9 (2022) 1518–1525.
[14] R. Li, P. Niu, T. Yuan, P. Cao, C. Chen, K. Zhou, J. Alloy. Compd. 746 (2018) 125–134.
[15] R. Zhou, Y. Liu, C. Zhou, S. Li, W. Wu, M. Song, B. Liu, X.P Liang, P.K. Liaw, Intermetallics 94 (2018) 165–171.
[16] Z. Fu, B. Yang, K. Gan, D. Yan, Z. Li, G. Gou, H. Chen, Z. Wang, Corros. Sci. 190 (2021) 109695.
[17] H. Duan, B. Liu, A. Fu, J. He, T. Yang, C.T. Liu, Y. Liu, J. Mater. Sci. Technol. 99 (2022) 207–214.
[18] H. Chen, Q. Fang, K. Zhou, Y. Liu, J. Li, CrystEngComm 22 (2020) 4136–4146.
[19] S. Kurian, R. Mirzaeifar, Addit. Manuf. 35 (2020) 101272.
[20] J. Li, H. Chen, S. Li, Q. Fang, Y. Liu, L. Liang, H. Wu, P.K. Liaw, Mater. Sci. Eng. A 760 (2019) 359–365.
[21] E. Liverani, S. Toschi, L. Ceschini, A. Fortunato, J. Mater. Process. Technol. 249 (2017) 255–263.
[22] H. Shipley, D. McDonnell, Culleton M, R. Coull, R. Lupoi, G. O'Donnell, D. Trimble, Int. J. Mach. Tool Manuf. 128 (2018) 1–20.
[23] W.M. Tucho, V.H. Lysne, H. Austbø, A. Sjolyst-Kverneland, V. Hansen, J. Alloy. Compd. 740 (2018) 910–925.
[24] R. Halonen, E. Zapadinsky, H. Vehkamäki, J. Chem. Phys. 148 (2018) 164508.
[25] Q. Spreiter, M. Walter, J. Comput. Phys. 152 (1999) 102–119.
[26] G. Bonny, N. Castin, D. Terentyev, Model. Simul. Mater. Sci. Eng. 21 (2013) 085004.
[27] G. Bonny, D. Terentyev, R.C. Pasianot, S. Poncé, A. Bakaev, Simul. Mater. Sci. Eng. 19 (2011) 085008.
[28] C. Varvenne, A. Luque, W.G. Nöhring, W.A. Curtin, Phys. Rev. B 93 (2016) 104201.
[29] O.N. Senkov, G.B. Wilks, D.B. Miracle, C.P. Chuang, P.K. Liaw, Intermetallics 18 (2010) 1758–1765.
[30] Y. Zhang, H. Liu, J. Mo, M. Wang, Z. Chen, Y. He, W. Yang, C. Tang, Comput. Mater. Sci. 150 (2018) 62–69.
[31] Z. Xiao, C. Chen, H. Zhu, Z. Hu, B. Nagarajan, L. Guo, X. Zeng, Mater. Des. 193 (2020) 108846.
[32] J. Li, Q. Fang, B. Liu, Y. Liu, Acta Mater. 147 (2018) 35–41.
[33] A. Stukowski, Model. Simul. Mater. Sci. Eng. 18 (2009) 015012.
[34] K. Kunze, T. Etter, J. Grässlin, V. Shklover, Mater. Sci. Eng. A 620 (2015) 213–222.
[35] J. Hou, W. Chen, Z. Chen, K. Zhang, A. Huang, J. Mater. Sci. Technol. 48 (2020) 63–71.
[36] Y. Hong, C. Zhou, Y. Zheng, L. Zhang, J. Zheng, Mater. Sci. Eng. A 799 (2021) 140279.
[37] Y. Wang, B. Liu, K. Yan, M. Wang, S. Kabra, Y.L. Chiu, D. Dye, P.D. Lee, B. Cai, Acta Mater. 154 (2018) 79–89.
[38] L. Li, Z. Li, A.K. da Silva, Z. Peng, H. Zhao, B. Gault, D. Raabe, Acta Mater. 178 (2019) 1–9.
[39] K.G. Prashanth, J. Eckert, J. Alloy. Compd. 707 (2017) 27–34.
[40] A. Fu, B. Liu, W. Lu, B. Liu, J. Li, Q. Fang, Z. Li, Y. Liu, Scr. Mater. 186 (2020) 381–386.
[41] J. Li, M. Yi, H. Wu, Q. Fang, Y. Liu, B. Liu, K. Zhou, P.K. Liaw, Mater. Sci. Eng. A 790 (2020) 139736.
[42] Y. Feng, X. Gao, Y. Zhang, C. Peng, X. Gui, Y. Sun, X. Xiao, Int. J. Adv. Manuf. Technol. 112 (2021) 2301–2312.
[43] D.R. Liu, S. Wang, W. Yan, Mater. Des. 194 (2020) 108919.
[44] D. Gu, C. Ma, M. Xia, D. Dai, Q. Shi, Engineering 3 (2017) 675–684.
[45] Z. Gao, Bu H, Y. Feng, F. Lyu, X. Zhan, J. Manuf. Process. 71 (2021) 37–55.
[46] Y.J. Gao, Q.Q. Deng, Z.Y. Liu, Z.J. Huang, Y.X. Li, Z.R. Luo, J. Mater. Sci. Technol. 49 (2020) 236–250.
[47] M.G. Tsoutsouva, G. Regula, B. Ryningen, P.E. Vullum, N. Mangelinck-Noël, G. Stokkan, Acta Mater. 210 (2021) 116819.
[48] S. Sunny, R. Mathews, G. Gleason, A. Malik, J. Halley, Int. J. Mech. Sci. 202 (2021) 106534.
[49] X. Li, H. Gao, Nat. Mater. 15 (2016) 373–374.
[50] Z.H. Cao, G.Y. Zhai, Y.J. Ma, L.P. Ding, P.F. Li, H.L. Liu, H.M. Lu, Y.P. Cai, X.K. Meng, Int. J. Plast. 145 (2021) 103081.
[51] Y.F. Zhao, X.B. Feng, J.Y. Zhang, Y. Lu, S.H. Wu, Y.Q. Wang, K. Wu, J. Sun, Nanoscale 12 (2020) 14135–14149.
[52] S.S. Sohn, A. Kwiatkowski da Silva, Y. Ikeda, F. Körmann, W. Lu, W.S. Choi, B. Gault, D. Ponge, J. Neugebauer, D. Raabe, Adv. Mater. 31 (2019) 1807142.
[53] A.R. Denton, N.W. Ashcroft, Phys. Rev. A 43 (1991) 3161.
[54] L. Li, Q. Fang, J. Li, B. Liu, Y. Liu, P.K. Liaw, Mater. Sci. Eng. A 784 (2020) 139323.
[55] Y.K. Kim, J. Choe, K.A. Lee, J. Alloy. Compd. 805 (2019) 680–691.
[56] H. Zhou, X. Li, S. Qu, W. Yang, H. Gao, Nano Lett. 14 (2014) 5075–5080.